

Document downloaded from:

<http://hdl.handle.net/10251/78196>

This paper must be cited as:

Martínez Casas, J.; Mazzola, L.; Baeza González, LM.; Bruni, S. (2013). Numerical Estimation of Stresses in Railway Axles Using a Train-Track Interaction Model. *International Journal of Fatigue*. 47:18-30. doi:10.1016/j.ijfatigue.2012.07.006.



The final publication is available at

<http://dx.doi.org/10.1016/j.ijfatigue.2012.07.006>

Copyright Elsevier

Additional Information

Numerical Estimation of Stresses in Railway Axles Using a Train-Track Interaction Model

Authors: José Martínez-Casas¹, Laura Mazzola², Luis Baeza¹, Stefano Bruni²

Affiliation:

¹Centro de Investigación en Tecnología de Vehículos, Universidad Politécnica de Valencia, Camino de Vera s/n, 46022 Valencia - Spain

²Dipartimento di Meccanica, Politecnico di Milano, Via La Masa 1, 20156 Milano, Italy

E-mail corresponding author: *stefano.bruni@mecc.polimi.it*

Abstract

The fatigue design of railway axles requires that the stresses arising in the axle in real service are accurately quantified. This paper describes a method to compute the dynamic stresses arising in railway axles as the effect of train-track interaction, based on the numerical simulation of the dynamic interaction between a flexible wheelset and a flexible track. The wheelset is modelled as a flexible rotating body using an Eulerian approach, whereas track is regarded as an infinite periodic system with the rail modelled as a Timoshenko beam resting on discrete elastic supports, considering the inertia associated with the sleepers.

The paper presents an application of the proposed procedure to the calculation of the dynamic stresses caused in the axle by different types of geometric imperfection occurring on the wheel and rail surfaces, considering the cases of a single harmonic rail corrugation, random rail roughness and a wheelflat.

Keywords

Railway vehicles, wheelset design, wheelset axle fatigue, dynamic loads, train-track interaction, rail roughness, wheelflat

1. Introduction

1
2 Railway axles durability is a key issue in designing and correctly maintaining railway vehicles, to
3
4 ensure that the highest safety standards are met and, at the same time, to optimise life-cycle costs
5
6 from a system point of view, i.e. considering not only the vehicle but also the interacting
7
8 infrastructure. From the single point of view of fatigue resistance, the axle design should tend
9
10 towards increasing the size to reduce stresses, but this component also represents a significant
11
12 contribution to the wheelset un-sprung mass, which, on the contrary, shall be minimised to reduce
13
14 the generation of dynamic force at wheel-rail contact and hence damage in the track and in the
15
16 wheels, especially for high-speed trains.
17
18
19

20
21 At present, wheelset axles are designed for infinite fatigue life, however a small number of axle
22
23 failures due to fatigue continues to be reported, sometimes with catastrophic consequences. One of
24
25 the reasons which have been proposed to explain these unforeseen failures is that the loads assumed
26
27 by the standard for the purpose of fatigue design verification do not fully reflect the actual service
28
29 loads of the vehicle, which are largely depending on the vehicle design parameters (e.g. unsprung
30
31 masses, suspension stiffness and damping, ...) and on the vehicle service profile [1, 2]. The precise
32
33 knowledge of service loads is also pivotal to the definition of appropriate intervals for the non-
34
35 destructive inspection of railway axles [3, 4], which are nowadays part of standard maintenance
36
37 practice to remove from service cracked axles before failure.
38
39
40
41
42
43
44
45

46 Detailed information on the service loads is often derived experimentally, using instrumented
47
48 wheelsets [5 - 7]. This approach however presents some drawbacks: first of all, the physical
49
50 measure is not applicable at the design stage of a new vehicle, setting-up and running the tests is
51
52 expensive and demanding due to the harsh measuring environment and extensive test campaigns are
53
54 required to cover all service conditions (different lines and speeds, operation at tare / full load, new
55
56 / worn wheel profiles, ...). Furthermore, the experimental measure of the service load is normally
57
58
59
60
61
62
63
64
65

1 not able to fully explain the causes of extreme loads, which result in stress peaks mostly affecting
2 the fatigue resistance of the axle and crack propagation.
3
4
5

6
7 For this reason, in the last year attempts have been made to define procedures based on the use of
8
9 multi-body models of a railway vehicle or train set, to provide a numerical estimate of the service
10 loads [6 – 8]. This approach can be used to complement measurements, e.g. addressing service
11 conditions not covered by the tests and to provide a better physical understanding of the factors
12 influencing the service spectra, including (among others) vehicle design parameters, the condition
13 of the wheel and rail surfaces and the service scenario. To the Authors' knowledge, these
14 approaches have however until now been developed considering the wheelset as a rigid body.
15
16

17 Hence, axle stresses can be correctly computed only in the low-frequency range (approximately 0-
18 20 Hz), whereas their high-frequency components, mainly responsible for the occurrence of stress
19 peaks, are excluded from the analysis [8].
20
21
22

23
24 This paper aims therefore at establishing a method to define numerically the stresses in a railway
25 axle, including the high frequency components, as function of vehicle-track parameters and of the
26 vehicle's running condition, thereby extending the scope and detail of the existing numerical
27 approaches to predict the wheelset service loads. To this end, a model of a flexible wheelset
28 interacting with a flexible track in tangent track is derived and used to simulate typical service
29 scenarios for a high-speed railway vehicle. The wheelset is modelled as a flexible rotating body,
30 using an Eulerian approach to take advantage from axial symmetry and modal synthesis to reduce
31 the size of the problem. The track is modelled as an infinite periodic system, with the rail modelled
32 as a Timoshenko beam resting on discrete elastic supports, considering the inertia associated with
33 the sleepers. The numerical simulation considers the effect of geometric irregularities appearing on
34 the rail and wheel surfaces, allowing to consider the effect of e.g. rail corrugation, rail dips, wheel
35 polygonalisation, wheel flats etc.
36
37
38
39
40
41
42
43
44
45
46
47
48
49
50
51
52
53
54
55
56
57
58
59
60
61
62
63
64
65

1
2
3
4
5
6
7
8
9
10
11
12
13
14
15
16
17
18
19
20
21
22
23
24
25
26
27
28
29
30
31
32
33
34
35
36
37
38
39
40
41
42
43
44
45
46
47
48
49
50
51
52
53
54
55
56
57
58
59
60
61
62
63
64
65

Train-track interaction models including a detailed description of the wheelset as an elastically deformable body have been proposed by several authors. Some models, e.g. [9] are defined in the frequency domain and derive the dynamic forces at wheel-rail contact by combining the wheelset and track frequency response functions with the assumed rail corrugation. This approach is inherently linear and does not allow to consider the rails as discretely supported. Modelling approaches which incorporate a discrete-support track model and the effect of nonlinearities in the track and in wheel-rail contact have been developed in Refs. [10–14]: in this case, the train-track model is defined in the time domain and the wheelset and track models are defined using the finite element method, introducing a reduction of the degrees of freedom using mode superposition.

These approaches have been mostly applied to the study of damage phenomena in the track and at wheel-rail interface, and therefore focus on the definition of wheel-rail contact forces rather than axle stresses. Therefore, a simplified model of the wheelset axle (sometimes based on beam elements) can be used. Furthermore, the effect of wheelset rotation is neglected or considered with some approximation, whereas this effect may importantly affect the wheelset resonance conditions, which in turn can be a cause of extreme stress peaks arising in the axle: the present paper aims therefore at developing a modelling and simulation approach specifically tailored on the prediction of axle stresses

The paper describes the wheelset-track interaction model developed and the procedure to compute the dynamic stresses in the axle. Results of the numerical procedure are presented for different excitation cases including rail corrugation having different wavelength and a wheelflat, and considering the effect of wheelset speed.

2. THE VEHICLE-TRACK INTERACTION MODEL

The vehicle – track interaction model, see Figure 1, is defined adopting a sub-structuring technique [15, 16], according to which the whole system is divided into substructures: the vehicle, the rails and the rail supports. For each substructure, the equations of motion are written separately, and interaction effects between vehicle and track are represented by the wheel-rail contact forces and by the forces generated at the railpads [15]. The simulation approach is developed considering the motion of the wheelset in tangent track.

Given the range of frequencies addressed, the vehicle model is confined to one wheelset with primary suspension, see section 2.1. The vibration of the flexible wheelset is expressed using Eulerian modal coordinates, see Section 3, taking advantage from the axial symmetry of the body. Furthermore the modal approach is chosen to describe the wheelset motion in order to reduce the computational effort required by the simulation.

The track is modelled by means of a cyclic approach, which provides some benefit with respect to classical track modelling or the finite one. The sub-structuring technique is still adopted here to simplify the system modelling; a detailed description of the track is provided in section 2.2.

2.1 The Vehicle Model

The dynamic stresses arising in the wheelset axle are mostly related with train-track interaction effects in the frequency range above 20 Hz, which are excited by short wavelength geometric imperfections in the wheel and rail profiles and by singularities such as rail dips and wheel flats.

In this frequency range the dynamics of the sprung masses (bogie frame and car body) are effectively isolated from the motion of the un-sprung masses (wheelsets and axle boxes) on account of the mechanical filter introduced by the suspensions. Therefore, the vehicle model used in this paper considers one single wheelset, modelled as an elastically flexible body, and the primary

1 suspension, represented using visco-elastic lumped parameter elements. The static load associated
2 with the gravitational forces acting on the bogie and on the carbody masses is represented by two
3 static forces applied through the primary suspension on the two sides of the wheelset.
4
5
6
7

8 9 **2.2 The Track Model**

10 The track is modelled by means of a cyclic approach, where a finite section of the track is defined,
11 introducing cyclic boundary conditions at the ends of the model, hence the track, see Figure 2, can
12 be interpreted as an infinite track, negotiated by an infinite set of identical vehicles, uniformly
13 distributed in such a way that each vehicle is set at a constant distance L apart from the adjacent
14 ones. Due to the periodicity of the structure and of the loading conditions, the study is reduced to a
15 single section having finite length L , whose value is set large enough to avoid interaction between
16 the vehicles.
17
18

19 The model adopted for the different track components is illustrated in Figure 3: the rails are
20 modelled as Timoshenko beams, including bending deformations in vertical/lateral directions, as
21 well as torsional deformations. Rail vibration is introduced in terms of modal superposition for the
22 unconstrained rail with cyclic boundary conditions, hence resulting into a set of de-coupled 1-d.o.f.
23 equations. Moreover due to the symmetry of the sub-system with respect to the track centreline,
24 only one rail is modelled in the present study.
25
26
27
28

29 The discrete rail supports are introduced in the form of lumped parameter systems, see Figure 3
30 right. The rail pads are modelled as lumped visco-elastic elements generating the interaction forces
31 between the rails and the sleepers, represented as lumped masses. Ballast dynamics is neglected
32 here, being not relevant for the stress analysis on the wheelset, but the equivalent ballast stiffness
33 and damping are accounted for by means of lumped spring and dashpot elements.
34
35
36
37
38
39
40
41
42
43
44
45
46
47
48
49
50
51
52
53
54
55
56
57
58
59
60
61
62
63
64
65

2.3 The Model of Wheel-Rail Contact Forces

The track model is coupled with the flexible wheelset via the wheel-rail contact forces, which are expressed as function of the relative wheel-rail displacement and velocity in the contact patch. In the numerical model presented here, the theory of Hertz is adopted to define the normal contact force component and FASTSIM [17] is used to define the tangential contact forces as function of the normal contact force and of the creepage components.

At each time step, the displacement and velocity of the wheel in the contact point are obtained using Eq. (1) evaluated at the contact point position.

3. THE FLEXIBLE WHEELSET MODEL

In order to model the kinematics of the flexible wheelset, two configurations (undeformed and deformed) are defined. The undeformed configuration is associated with the spinning velocity of the wheelset (at constant angular velocity Ω). The deformed configuration considers the flexibility and small rigid solid displacements. The displacement field relates the deformed configuration with the undeformed configuration as it will be shown in Eq. (1).

The coordinates that are implemented in the wheelset model do not follow the material points of the solid which is the commonest procedure in Mechanics, nevertheless they are associated with spatial points (Eulerian approach). Let \mathbf{u} an Eulerian vector coordinate in a fixed coordinate frame. Any property of the solid $\varphi(\mathbf{u}, t)$ corresponds to the material point of the solid whose undeformed configuration is in the spatial point \mathbf{u} at instant t . Following this criterion, the displacement field is defined by means of the following formula:

$$\mathbf{r} = \mathbf{u} + \mathbf{w}(\mathbf{u}, t), \quad (1)$$

where \mathbf{r} is the final position of the particle, and \mathbf{w} is the displacements associated with flexibility and small rigid body displacements.

The coordinate frame is chosen so that the spin rotation is in the second axle. The following matrices are defined as follows:

$$\mathbf{J} = \begin{pmatrix} 0 & 0 & 1 \\ 0 & 0 & 0 \\ -1 & 0 & 0 \end{pmatrix}; \quad \mathbf{E} = \begin{pmatrix} 1 & 0 & 0 \\ 0 & 0 & 0 \\ 0 & 0 & 1 \end{pmatrix}. \quad (2)$$

The angular velocity tensor verifies:

$$\tilde{\Omega} = \begin{pmatrix} 0 & 0 & \Omega \\ 0 & 0 & 0 \\ -\Omega & 0 & 0 \end{pmatrix} = \Omega \mathbf{J}; \quad \text{and} \quad \tilde{\Omega} \tilde{\Omega} = -\Omega^2 \mathbf{E}. \quad (3)$$

The velocity due to the rigid body spinning is:

$$\mathbf{v} = (v_1 \quad v_2 \quad v_3)^T = \tilde{\Omega} \mathbf{u} = \Omega \mathbf{J} \mathbf{u} = \Omega \tilde{\mathbf{u}}, \quad (4)$$

where $\tilde{\mathbf{u}} = (u_3 \quad 0 \quad -u_1)^T$. The velocity of the particle is computed through the material derivative of \mathbf{r} , and that is

$$\frac{D\mathbf{r}}{Dt} = \frac{D\mathbf{u}}{Dt} + \frac{D\mathbf{w}}{Dt} = \sum_i v_i \frac{\partial \mathbf{u}}{\partial u_i} + \dot{\mathbf{w}} + \sum_i v_i \frac{\partial \mathbf{w}}{\partial u_i} = \Omega \mathbf{J} \mathbf{u} + \dot{\mathbf{w}} + \Omega \sum_i \tilde{u}_i \frac{\partial \mathbf{w}}{\partial u_i}. \quad (5)$$

In order to calculate the kinetic energy of the solid, the square of the particle velocity Eq. (5) has to be obtained. It has the following formula:

$$\begin{aligned} \frac{D\mathbf{r}^T}{Dt} \frac{D\mathbf{r}}{Dt} &= \Omega^2 \mathbf{u}^T \mathbf{E} \mathbf{u} + \dot{\mathbf{w}}^T \dot{\mathbf{w}} + \Omega^2 \left(\sum_i \tilde{u}_i \frac{\partial \mathbf{w}^T}{\partial u_i} \right) \left(\sum_i \tilde{u}_i \frac{\partial \mathbf{w}}{\partial u_i} \right) \\ &+ 2\Omega \dot{\mathbf{w}}^T \mathbf{J} \mathbf{u} + 2\Omega^2 \left(\sum_i \tilde{u}_i \frac{\partial \mathbf{w}^T}{\partial u_i} \right) \mathbf{J} \mathbf{u} + 2\Omega \dot{\mathbf{w}}^T \left(\sum_i \tilde{u}_i \frac{\partial \mathbf{w}}{\partial u_i} \right). \end{aligned} \quad (6)$$

The next modal approach is adopted:

$$\mathbf{w}(\mathbf{u}, t) = \Phi(\mathbf{u}) \mathbf{q}(t), \quad (7)$$

being $\Phi(\mathbf{u})$ the mode shape functions matrix of the free-boundary wheelset. The small rigid displacements of the solid are considered in this approach through the rigid modes of the wheelset.

It must be pointed out that the mode shape functions do not depend on time since the rotation of the solid does not change the mode shapes functions in fixed coordinates, because the axial symmetry

of the wheelset. The use of the mode shapes in fixed coordinates as basis function when the solid is in motion is called Eulerian modal approach. Once the formula Eq. (7) is applied in Eq.(6), the kinetic energy results in the following expression:

$$\begin{aligned}
E_k &= \frac{1}{2} \int_{Vol} \rho \frac{D\mathbf{r}}{Dt} \frac{D\mathbf{r}}{Dt} dV = \frac{1}{2} \dot{\mathbf{q}}^T \int_{Vol} \rho \Phi^T \Phi dV \dot{\mathbf{q}} + \frac{1}{2} \Omega^2 \int_{Vol} \rho \mathbf{u}^T \mathbf{E} \mathbf{u} dV \\
&+ \frac{1}{2} \Omega^2 \mathbf{q}^T \int_{Vol} \rho \left(\sum_i \tilde{u}_i \frac{\partial \Phi^T}{\partial u_i} \right) \left(\sum_i \tilde{u}_i \frac{\partial \Phi}{\partial u_i} \right) dV \mathbf{q} + \Omega \dot{\mathbf{q}}^T \int_{Vol} \rho \Phi^T \mathbf{J} \mathbf{u} dV \\
&+ \Omega^2 \mathbf{q}^T \int_{Vol} \rho \left(\sum_i \tilde{u}_i \frac{\partial \Phi^T}{\partial u_i} \right) \mathbf{J} \mathbf{u} dV + \Omega \dot{\mathbf{q}}^T \int_{Vol} \rho \Phi^T \left(\sum_i \tilde{u}_i \frac{\partial \Phi}{\partial u_i} \right) dV \mathbf{q}.
\end{aligned} \tag{8}$$

Two terms of Lagrange's equation are computed as follows:

$$\begin{aligned}
\frac{D}{Dt} \left(\frac{\partial E_k}{\partial \dot{\mathbf{q}}} \right)^T &= \int_{Vol} \rho \Phi^T \Phi dV \ddot{\mathbf{q}} + \Omega \int_{Vol} \rho \Phi^T \left(\sum_i \tilde{u}_i \frac{\partial \Phi}{\partial u_i} \right) dV \dot{\mathbf{q}} - \Omega^2 \int_{Vol} \rho \Phi^T \mathbf{E} \mathbf{u} dV \\
&+ \Omega \int_{Vol} \rho \left(\sum_i \tilde{u}_i \frac{\partial \Phi^T}{\partial u_i} \right) \Phi dV \dot{\mathbf{q}} + \Omega \int_{Vol} \rho \Phi^T \left(\sum_i \tilde{u}_i \frac{\partial \Phi}{\partial u_i} \right) dV \dot{\mathbf{q}} \\
&+ \Omega^2 \int_{Vol} \rho \left(\sum_i \tilde{u}_i \frac{\partial \Phi^T}{\partial u_i} \right) \mathbf{J} \mathbf{u} dV - \Omega^2 \int_{Vol} \rho \Phi^T \left(\sum_{i=1,3} u_i \frac{\partial \Phi}{\partial u_i} \right) dV \mathbf{q} \\
&+ \Omega^2 \int_{Vol} \rho \left(\sum_i \tilde{u}_i \frac{\partial \Phi^T}{\partial u_i} \right) \left(\sum_i \tilde{u}_i \frac{\partial \Phi}{\partial u_i} \right) dV \mathbf{q} + \Omega^2 \int_{Vol} \rho \Phi^T \left(\sum_j \sum_i \tilde{u}_i \tilde{u}_j \frac{\partial^2 \Phi}{\partial u_i \partial u_j} \right) dV \mathbf{q}
\end{aligned} \tag{9}$$

$$\begin{aligned}
\left(\frac{\partial E_k}{\partial \mathbf{q}} \right)^T &= \Omega^2 \int_{Vol} \rho \left(\sum_i \tilde{u}_i \frac{\partial \Phi^T}{\partial u_i} \right) \left(\sum_i \tilde{u}_i \frac{\partial \Phi}{\partial u_i} \right) dV \mathbf{q} \\
&+ \Omega^2 \int_{Vol} \rho \left(\sum_i \tilde{u}_i \frac{\partial \Phi^T}{\partial u_i} \right) \mathbf{J} \mathbf{u} dV + \Omega \int_{Vol} \rho \left(\sum_i \tilde{u}_i \frac{\partial \Phi^T}{\partial u_i} \right) \Phi dV \dot{\mathbf{q}}
\end{aligned} \tag{10}$$

Finally, the equation of motion is obtained:

$$\begin{aligned}
\frac{D}{Dt} \left(\frac{\partial E_k}{\partial \dot{\mathbf{q}}} \right)^T - \left(\frac{\partial E_k}{\partial \mathbf{q}} \right)^T &= \ddot{\mathbf{q}} + 2\Omega \int_{Vol} \rho \Phi^T \left(\sum_i \tilde{u}_i \frac{\partial \Phi}{\partial u_i} \right) dV \dot{\mathbf{q}} + \Omega^2 \int_{Vol} \rho \Phi^T \left(\sum_j \sum_i \tilde{u}_i \tilde{u}_j \frac{\partial^2 \Phi}{\partial u_i \partial u_j} \right) dV \mathbf{q} \\
&- \Omega^2 \int_{Vol} \rho \Phi^T \left(\sum_{i=1,3} u_i \frac{\partial \Phi}{\partial u_i} \right) dV \mathbf{q} - \Omega^2 \int_{Vol} \rho \Phi^T \mathbf{E} \mathbf{u} dV.
\end{aligned} \tag{11}$$

The modal properties are computed from a finite element (FE) model, therefore it is convenient to use the FE methodology for computing the equation of motion numerically. The mode shape functions are obtained into the e -th element of the FE mesh as follows

$$\mathbf{\Phi}(\mathbf{u}) = \mathbf{N}^e(\mathbf{u}) \mathbf{\Phi}_{FE}^e, \quad (12)$$

being $\mathbf{N}^e(\mathbf{u})$ the basis function matrix of the e -th element, and $\mathbf{\Phi}_{FE}^e$ the mode shapes computed in the nodes of the e -th element through the FE model.

One first step in the FE method is to compute each integral on the volume of the solid as the sum of integrals on the volume of the FE elements, that is:

$$\int_{Vol} \bullet dV = \sum_{elements} \int_{Vol^e} \bullet dV. \quad (13)$$

This approach can be performed if the integrand is bounded in the element edges. Once this step is complete, the method is centred on obtaining the matrices of the elements. These matrices have to be assembled in global matrices, following the standard FE assembling technique. The first matrix of the element in Eq. (11) is obtained by means of the approach in Eq. (12) as follows:

$$2\Omega \int_{Vol^e} \rho \mathbf{\Phi}^T \left(\sum_i \tilde{u}_i \frac{\partial \mathbf{\Phi}}{\partial u_i} \right) dV = 2\Omega \mathbf{\Phi}_{FE}^{eT} \int_{Vol^e} \rho \mathbf{N}^{eT} \left(\sum_i \tilde{u}_i \frac{\partial \mathbf{N}^e}{\partial u_i} \right) dV \mathbf{\Phi}_{FE}^e, \quad (14)$$

being defined \mathbf{V}^e as the corresponding matrix of the element, that is:

$$\mathbf{V}^e = \int_{Vol^e} \rho \mathbf{N}^{eT} \left(\sum_i \tilde{u}_i \frac{\partial \mathbf{N}^e}{\partial u_i} \right) dV. \quad (15)$$

Following the same procedure than Eq. (14), the remaining matrices of the elements are obtained :

$$\mathbf{A}^e = \int_{Vol^e} \rho \mathbf{N}^{eT} \left(\sum_j \sum_i \tilde{u}_i \tilde{u}_j \frac{\partial^2 \mathbf{N}^e}{\partial u_i \partial u_j} \right) dV, \quad (16)$$

$$\mathbf{C}^e = \int_{Vol^e} \rho \mathbf{N}^{eT} \left(\sum_{i=1,3} u_i \frac{\partial \mathbf{N}^e}{\partial u_i} \right) dV, \quad (17)$$

$$\mathbf{c}^e = \int_{Vol^e} \rho \mathbf{N}^{eT} \mathbf{E} \mathbf{u} dV. \quad (18)$$

The term where \mathbf{V}^e appears can be identified as inertial force due to Coriolis acceleration associated with the convective velocity. Matrix \mathbf{A}^e is related to convective acceleration. Matrix \mathbf{C}^e is associated with centrifugal forces that appear after deformation of the solid. Finally, column

1 matrix \mathbf{c}^e corresponds to constant centrifugal forces. Integrals in Eqs. (15) to (18) are computed
2 numerically following Gauss quadrature.
3
4
5
6

7 The presence of the second derivative in Eq. (16) does not guarantee the convergence to the integral
8 (because there is C^0 continuity between FE elements). However, the convergence can be proved if
9 one integrates Eq. (16) by parts.
10
11
12

13 The terms of Lagrange's equation related with non - conservative forces and elastic energy are
14 computed like standard modal approach procedure (because Eulerian displacements and virtual
15 displacements do not depend on time). The matrices of the elements (e.g. \mathbf{A}^e) are assembled into
16 the global matrices (giving matrix \mathbf{A}), and the following equation of motion is found
17
18
19
20
21
22

$$23 \quad \ddot{\mathbf{q}} + 2\Omega \mathbf{\Phi}_{FE}^T \mathbf{V} \mathbf{\Phi}_{FE} \dot{\mathbf{q}} + (\mathbf{D} + \Omega^2 \mathbf{\Phi}_{FE}^T (\mathbf{A} - \mathbf{C}) \mathbf{\Phi}_{FE}) \mathbf{q} = \Omega^2 \mathbf{\Phi}_{FE}^T \mathbf{c} + \mathbf{Q}, \quad (19)$$

24 being \mathbf{Q} the generalized forces, and \mathbf{D} a diagonal matrix that contains the square of the undamped
25 natural frequencies of the free-boundary solid.
26
27
28
29
30
31

32 33 34 **3.1 Calculation of Stresses in the Wheelset**

35 The simulation of train-track interaction is finalized in this paper towards the calculation of
36 dynamic stresses arising in the wheelset axle. To perform the stress calculation, first of all some
37 sections of interest are identified along the axle. These sections were chosen sufficiently far from
38 diameter changes, to avoid stress concentration effects which cannot be captured with the simple
39 mesh adopted, see Figure 4. In this paper, results are reported for one single section of the axle,
40 which is set at mid distance between the central brake disk and one of the side brake disks, see
41 Figure 5.
42
43
44
45
46
47
48
49
50
51
52

53 In order to derive the dynamic stresses, the simulation results in terms of the Eulerian modal
54 coordinates vector $\mathbf{q}(t)$ are processed according to Eq. (1) to derive the strains and stresses in
55 different spatial points along the exterior surface of the considered axle section. Then, one material
56
57
58
59
60
61
62
63
64
65

1 point is chosen in the section and followed during the rotation of the wheelset, to derive the time
2 history of the stress in the selected point.
3
4
5

6 7 **4. RESULTS** 8

9 In this section, results of train-track interaction calculations are shown considering different sources
10 of excitation: a single harmonic rail corrugation, random rail roughness and a wheelflat. The case
11 study considered here refers to the trailed car of a concentrated power train for high-speed
12 passenger service. The vehicle is equipped with a solid axle wheelset with monobloc, light design
13 wheels. The track considered features UIC60 rails and track parameters are based on the
14 EUROBALT project, considering a “stiff” track.
15
16
17
18
19
20
21
22

23
24
25
26 Table 1 summarises the input data used to set-up the simulation model. In all analyses reported
27 below (unless those considering the wheelset as a rigid body), the first 100 modes of vibration of
28 the flexible wheelset are considered, covering the frequency range up to 2.7 kHz approximately.
29
30
31
32

33
34
35
36 Results are shown starting from the simple excitation case represented by a single harmonic rail
37 corrugation and then extended to the cases of random rail corrugation and wheelflat.
38
39
40
41
42

43 **4.1 Results for single harmonic rail corrugation** 44

45 The first excitation case considered is rail corrugation having sinusoidal waveform. Different
46 corrugation wavelengths are considered, including values exciting some resonances of the track and
47 wheelset. The first case considered refers to a corrugation wavelength of 60 mm (i.e. one tenth of
48 the sleeper bay). In Figure 6 the vertical contact force generated by the wheelset travelling on the
49 corrugated rail is plotted as function of the distance travelled for different vehicle speeds (100 and
50 300 km/h) and for different corrugation amplitudes. In the upper subfigure, a corrugation peak-to-
51 peak depth of 4.84 μm is considered, corresponding to the limit amplitude defined by the ISO 3095
52
53
54
55
56
57
58
59
60
61
62
63
64
65

1 standard. For the higher speed, the result obtained for the case of a rigid wheelset (i.e. excluding
2 from the analysis all modes except the rigid ones) is also shown, to evaluate the effect of wheelset
3 flexibility. Finally, the rail roughness profile is also reported in the figure using an appropriate
4 scaling and offset to obtain a proper visualisation.
5
6
7
8
9

10
11 Two harmonic contents are observed in the vertical contact force, the largest one having the same
12 wavelength as the rail corrugation and a second one with wavelength equal to the sleeper bay. This
13 second harmonic component is due to the periodic variation of the rail stiffness seen by the wheelset
14 as the consequence of the discrete rail support. The amplitude of the dynamic contact force
15 component having the same wavelength as the corrugation is highly influenced by the wheelset
16 speed, being approximately three times greater at 300 km/h than at 100 km/h. The contact force is
17 also highly affected by wheelset flexibility: the comparison of the results obtained for the rigid and
18 flexible wheelset at the speed of 300 km/h shows that neglecting wheelset flexibility leads to over-
19 estimating the peak-to-peak amplitude of the dynamic force by 25% approximately. This is due to
20 the fact that at the considered excitation frequency of 1390 Hz approximately (corresponding to the
21 ratio of the wheelset speed over the corrugation wavelength) the wheelset mass participating to the
22 vertical motion is lower than the whole mass of the wheelset due to flexibility effects, a mechanism
23 which is not captured by the rigid wheelset model.
24
25
26
27
28
29
30
31
32
33
34
35
36
37
38
39
40
41
42
43
44
45

46 The corrugation peak-peak amplitude of 4.84 μm is relatively small compared to the typical
47 amplitude of rail corrugation, which is in the range of tens or even hundreds of μm . Indeed,
48 ISO 3095 limit is defined for a random corrugated profile including several wavelengths which
49 altogether would lead to a greater peak-peak amplitude. Therefore, in the lower subfigure of Figure
50 6 the vertical contact force obtained for the flexible wheelset at 300 km/h is compared for two
51 corrugation amplitudes, one corresponding to the ISO 3095 limit (same as in the upper subfigure)
52 and the other ten times greater; this comparison also allows to assess the importance of non-linear
53
54
55
56
57
58
59
60
61
62
63
64
65

1 effects in the case considered. For the larger corrugation amplitude, the peak-to peak amplitude of
2 the vertical force is approximately 93 kN, and leads to a maximum wheel overloading / unloading
3 which is approximately 78% of the static load. For the case considered here, non-linear effects
4 appear to play a relatively marginal role, since the maximum dynamic variation of the vertical load
5 for the larger corrugation amplitude is with good approximation ten times greater than for the small
6 corrugation amplitude. However, the force fluctuation component having the same wavelength as
7 the sleeper bay is in this case less visible (note that the amplitude of excitation associated with this
8 effect does not change with the corrugation amplitude).
9
10
11
12
13
14
15
16
17
18
19
20

21 Figure 7 shows the y-axis normal stress in the studied section of the axle (cfr. Fig. 5), plotted as
22 function of the wheelset rotation for the same cases considered in Figure 6. On the left, the effect of
23 vehicle speed is analysed by comparing the results obtained at 100 and 300 km/h for the same
24 corrugation amplitude corresponding to the ISO 3095 limit: the waveform of the stress is with good
25 approximation sinusoidal with 2π periodicity, and the peak-peak amplitude is increased from
26 78.3 MPa to 88 MPa when the speed is increased from 100 to 300 km/h. On the right, the effect of
27 corrugation amplitude is considered by comparing the two results obtained for the two corrugation
28 amplitudes considered in Figure 6 at 300 km/h speed: these results are so close to each other that
29 cannot be distinguished, showing that the corrugation amplitude, despite highly affecting the
30 dynamic variation of the contact force (see Figure 6) bears almost no effect on the amplitude of the
31 axial stresses.
32
33
34
35
36
37
38
39
40
41
42
43
44
45
46
47

48 In Figure 8 the vertical wheel-rail contact forces obtained for single harmonic corrugation are
49 compared for the same vehicle speed (300 km/h) and for different corrugation wavelengths and
50 amplitudes: in particular, the upper subfigure shows the results obtained for a corrugation
51 wavelength exciting the pinned-pinned resonance of the track [15], considering two corrugation
52 amplitudes, one corresponding to the ISO 3095 limit and the other ten times greater. The peak-peak
53
54
55
56
57
58
59
60
61
62
63
64
65

1 amplitude of the dynamic force fluctuation is approximately 81 kN, and is therefore considerably
2 lower than for the 60 mm wavelength (cfr. Fig. 6), on account of the rail showing a greater mobility
3
4 in this resonance condition. Also in this case, the peak-peak force amplitude is nearly proportional
5
6 to the corrugation amplitude.
7
8
9

10
11 The lower subfigure shows the vertical contact force plotted vs. the travelled distance for a
12
13 corrugation wavelength exciting the first forward bending mode of the wheelset. In this case, the
14
15 peak-peak amplitude of the contact force for the larger corrugation amplitude is 82.2 kN, again
16
17 significantly lower than for the 60 mm wavelength. In this second case however the increase of the
18
19 peak-peak force amplitude with the corrugation amplitude is significantly less than proportional,
20
21 and also the waveform of the contact force is different for the two corrugation amplitudes: this shall
22
23 be ascribed to the different importance of the sleeper-passing effect in the two cases, rather than to
24
25 the effect of non-linearities.
26
27
28
29
30

31
32
33 In Figure 9, the y-axis normal stress in the axle is shown for the same cases as in Fig. 8. For the
34
35 corrugation wavelength exciting the pinned-pinned resonance of the track, no significant difference
36
37 is observed with respect to the cases reported in Figure 7 for the same speed (300 km/h), and again
38
39 an increase of the corrugation amplitude leaves unaffected the amplitude of the axial stress.
40
41
42

43 However, when the corrugation wavelength exciting the wheelset resonance and the large
44
45 corrugation amplitude is considered, the stress amplitude becomes 33% higher than in Figure 7
46
47 (despite the contact force being lower in this case than for the 60 mm wavelength) and deviates
48
49 significantly from the sinusoidal waveform. This result is justified by the effect of wheelset
50
51 flexibility playing a particularly important role in the case considered, on account of one mode of
52
53 vibration being excited in resonance.
54
55
56
57
58
59
60
61
62
63
64
65

1 A useful parameter to quantify the relevance of dynamic effects affecting the wheel-rail contact
2 forces and the stresses in the axle is the dynamic factor, defined as the ratio between the maximum
3 dynamic value of the quantity considered and the corresponding static value. For the contact force,
4
5 the dynamic factor k_Q is defined according to the following equation:
6
7

$$8 \quad k_Q = \frac{Q_{d,max}}{Q_s} \quad (20)$$

9
10 with $Q_{d,max}$ the maximum value of the contact force and Q_s the static wheel load. For the stress in
11
12 the axle the dynamic factor k_σ is defined as:
13
14

$$15 \quad k_\sigma = \frac{\sigma_{d,max}}{\sigma_{s,max}} \quad (21)$$

16 with $\sigma_{d,max}$ maximum dynamic stress in the material point considered and $\sigma_{s,max}$ the
17
18 corresponding maximum stress under the action of rotating bending produced by the static loads
19
20 acting on the wheelset.
21
22
23

24 In Figure 10 the dynamic factors k_Q and k_σ are reported as function of the vehicle speed for the
25
26 different types of rail corrugation presented above, considering a corrugation amplitude ten times
27
28 greater than the ISO 3095 limit; in this case, also the results for a corrugation wavelength exciting
29
30 the second forward bending mode of the wheelset are presented. For the contact force dynamic
31
32 factor k_Q , in the entire speed range considered, the largest values are obtained for the corrugation
33
34 wavelength exciting the first forward bending mode of the wheelset, with a maximum value close to
35
36 1.8. A local maximum appears for most of the corrugation cases considered for speeds in the 125-
37
38 135 km/h range, this is due to a resonance effect associated with the sleeper passing frequency that
39
40 excites P2 frequency (see P1 and P2 frequencies in Ref. [15]).
41
42
43
44
45
46
47
48
49
50
51
52
53
54
55
56
57
58
59
60
61
62
63
64
65

1
2
3
4
5
6
7
8
9
10
11
12
13
14
15
16
17
18
19
20
21
22
23
24
25
26
27
28
29
30
31
32
33
34
35
36
37
38
39
40
41
42
43
44
45
46
47
48
49
50
51
52
53
54
55
56
57
58
59
60
61
62
63
64
65

-As far as the stress dynamic factor k_{σ} is concerned, very similar trends and values are obtained for the case with no roughness, for roughness wavelength exciting the pinned-pinned frequency, leading to low values of stress amplification (max. value below 1.2). ~~Only Otherwise, in the case of the for~~ corrugation wavelength exciting ~~one of the wheelset the bending~~ resonances ~~of the wheelset~~ the stress dynamic factor is significantly higher and ~~can be reaches a maximum value close up~~ to about 1.8 for the case of corrugation wavelength exciting, with the resonance of the first forward and up to 1.4 approximately for corrugation wavelength exciting bending mode leading to larger dynamic stresses than for the second forward bending mode. The trends with speed are close to monotonically increasing, and the effect of the resonance associated with the sleeper passing is less evident than in the trend of the k_Q dynamic factor.

These results suggest that the bending stresses in the axle are highly affected by the wavelength of rail corrugation, and that combinations of train speed and corrugation wavelength leading to a resonance of a bending mode may be especially relevant in view of axle resistance to fatigue.

Particularly significant in view of real applications is the case of rail corrugation, a form of irregular wear of the rail often appearing in railway systems and characterised quasi-harmonic wear patterns developing on the rail head in longitudinal direction [18]. Corrugation wavelength can range from 50 mm or less up to more than 1m in the case of heavy haul corrugation, and typical wear depth values are in the range of some tenths of millimetre.

To quantify the relevance to fatigue of rail corrugation, we note that the design methods prescribed for railway axles by the European Standards EN13103 and EN13104 [19, 20] assume a 1.25 dynamic amplification factor on the loads generated at the primary suspension. Since the calculation of the bending stresses is then based on static equilibrium, also the bending stresses are magnified by 25% with respect to the static case, whereas the results in Figure 10 suggest that larger dynamic factors might apply when a particular combination of corrugation wavelength and train speed

excites one bending mode. For instance, a sinusoidal rail corrugation having approximately 350 mm wavelength and 0.15 mm depth (i.e. ten times the ISO3095 limit for the considered wavelength) would produce a dynamic stress amplification close to 40%. It shall be pointed out however that the equivalent static loads prescribed by EN13103/104 also include lateral wheel-rail contact forces due to curving, which are not included in the analysis presented here.

4.2 Results for random rail corrugation and for a wheelflat

The simple excitation cases considered in Sub-section 4.1 allow to point out the influence of different dynamic effects on train-track interaction and on the stresses in the wheelset, but do not represent realistic excitation cases. In this Sub-section, two sources of excitation typically occurring in serviced trains are considered: random rail roughness and a wheelflat. Random roughness takes place on the rail head on account of different causes: geometric imperfections associated with the manufacturing and installation of the rail, irregular wear caused by train passage and, for larger wavelengths, non-uniform track settlement due to permanent deformations in the soil and ballast (in this case, the term “track irregularities” is used instead of corrugation). Studies have shown that rail roughness and track irregularity take the form of stationary random processes characterised by their power spectral density, which can be defined based on the quality of track maintenance [2181]. On the other hand, wheelflats are localised defects occurring on the wheel surface as the result of full slip of the wheel, typically caused by poorly adjusted or faulty brakes [4922].

Figure 11 shows the vertical contact force plotted vs. the travelled distance for the train speeds of 100 and 300 km/h, considering the excitation produced by random rail corrugation (amplitude corresponding to the ISO 3095 limit). The results obtained considering a rigid and flexible wheelset model are compared. Important dynamic fluctuations of the contact force are evidenced, with the maximum dynamic value corresponding to approximately 1.6 times the static load. The differences

1 between the results obtained for the rigid and flexible wheelset are relatively small in this case, and
2 do not affect significantly the maximum contact force value.
3

4 Figure 12 presents the vertical contact force vs. travelled distance for a vehicle affected by a
5 wheelflat. The calculation has been carried out for 50 and 300 km/h by means of the rigid and
6 enhanced wheelset models. A severe dynamic effect is observed, consisting of the complete loss of
7 contact between the wheel and the rail, followed by an impact leading to a maximum value of the
8 contact force which is between 3 and 4 times the static load and finally by a transient vibration. The
9 differences between the results for the rigid and flexible wheelset model are small in terms of
10 duration of the contact loss and of maximum overloading, but the transient following the impact is
11 affected quite remarkably by wheelset flexibility, as demonstrated by the different frequency
12 contents of the contact force signal, see particularly the zoomed view on the right side of the figure.
13
14
15
16
17
18
19
20
21
22
23
24
25
26
27
28

29 The y-axis stresses for the random rail corrugation and wheelflat excitation cases are shown in
30 Figure 13. In the random corrugation case, the dynamic fluctuations of the stress component are
31 relatively low and lead to a maximum peak-peak stress amplitude around 91.2 MPa, corresponding
32 to a dynamic amplification with respect to the maximum stress produced by the static load k_{σ} of
33 1.18 approximately. When the wheelflat defect is considered, the results are highly affected by the
34 vehicle speed, with large dynamic effects taking place at low speed (with a dynamic factor k_{σ} of
35 1.34 approximately) on account of the repeated loss of contact of the wheel to the rail, and with a
36 reduction of the dynamic stresses at higher speed.
37
38
39
40
41
42
43
44
45
46
47
48
49
50

51 Finally, in Figure 14 the dynamic factors k_Q and k_{σ} are reported for the random corrugation and
52 wheelflat as function of the vehicle speed. The contact force dynamic factor k_Q is nearly
53 monotonically increasing up to a maximum value close to 1.8 for random corrugation excitation,
54 whereas in case of wheelflat excitation the dynamic factor is much higher, in the range of 2.8-4.2,
55
56
57
58
59
60
61
62
63
64
65

1 with larger values occurring at lower speeds: this is because at low speed the duration of the contact
2 loss caused by the wheelflat is longer and hence the following impact is larger. The stress dynamic
3 factor k_{σ} for the random corrugation excitation case is almost monotonically increasing with speed,
4 with a maximum value close to 1.3. For the wheelflat excitation case, a completely different trend is
5 observed, the stress dynamic factor k_{σ} being initially decreasing with the speed and then increasing
6 above 200 km/h. The maximum value of the stress dynamic factor for this excitation case is
7 obtained at the lowest speed considered in the analysis and is slightly below 1.5.
8
9

10 As in the case of excitation generated by a single-harmonic rail corrugation, it is interesting to
11 observe that in some cases the dynamic factor k_{σ} exceeds the 1.25 value assumed in EN13103/104.
12

13 For wheelflat excitation, this happens at low speeds (below 75 km/h) which are typical e.g. of
14 freight application whereas for random rail roughness the 1.25 value is exceeded only at very high
15 speeds above 300 km/h, which are only relevant to very high speed trains. It shall be stressed
16 however that the results shown in Figure 14 depend on the amplitude of the defects being
17 considered and, in case of more severe irregularities, larger dynamic stresses shall be expected.
18

19 It is also interesting to point out that by using a static calculation to derive the bending stresses,
20 Standards EN13103/104 inherently imply a proportionality between the contact forces and the
21 stresses, whereas the results in figures 10 and 14 show that the stress dynamic factor k_{σ} is
22 generally lower (sometimes much lower) than the dynamic factor for the vertical contact force k_Q .
23

24 This circumstance is due to the inertia forces generated in the wheels and to the different
25 magnification of wheelset flexible modes produced when resonance conditions occur and suggests
26 that a method based on a static calculation could be not fully suited to estimate service stresses in
27 the axle. Dynamic train-track interaction models such as the one proposed in this paper could be
28 envisaged as a means to derive a more realistic estimate of service stresses in the axle, but this
29
30
31
32
33
34
35
36
37
38
39
40
41
42
43
44
45
46
47
48
49
50
51
52
53
54
55
56
57
58
59
60
61
62
63
64
65

1 requires the study to be extended to consider the effect of curving, which is envisaged as a next
2 development of the work described here.
3
4

5 :-
6
7

8 9 **5. CONCLUSIONS**

10
11 Dynamic effects may be extremely important in determining the fatigue resistance of railway axles,
12 and need to be properly considered in the axle design process. This paper has presented a method
13 for the numerical estimation of the dynamic stresses in railway axles, based on the simulation of the
14 interaction between a flexible wheelset and a flexible track. The method is presently limited to the
15 case of tangent track running of the wheelset, but the extension to the curving condition is
16 envisaged as a next step of the research, to consider the additional axle loading due to wheel-rail
17 contact forces in a curve.
18
19

20
21 Results of the numerical procedures were presented in the paper, considering the dynamic excitation
22 caused by rail corrugation and by a wheelflat for different wheelset speed values. The results clearly
23 show that dynamic effects may lead to a significant dynamic amplification of the stresses in the
24 axle, which is in some cases close to 70%. However, the actual relevance of dynamic effects
25 affecting axle stresses is strongly depending upon the type of excitation and the vehicle speed.
26
27

28
29 When single harmonic corrugation is considered, the dynamic amplification of axle stresses is
30 relatively low except in the case when the corrugation wavelength excites the bending modes of the
31 wheelset. In the case of random multi-harmonic rail corrugation, the dynamic amplification factors
32 are relatively low because the excitation is spread over a wide range of frequencies, thus reducing
33 the importance of resonance effects. In all rail corrugation cases considered, regardless the
34 waveform of the excitation, the dynamic stress amplification tends to increase with the vehicle
35 speed, so that the most critical case is obtained for high-speed applications.
36
37
38
39
40
41
42
43
44
45
46
47
48
49
50
51
52
53
54
55
56
57
58
59
60
61
62
63
64
65

1
2
3
4
5
6
7
8
9
10
11
12
13
14
15
16
17
18
19
20
21
22
23
24
25
26
27
28
29
30
31
32
33
34
35
36
37
38
39
40
41
42
43
44
45
46
47
48
49
50
51
52
53
54
55
56
57
58
59
60
61
62
63
64
65

Wheel flat excitation also appears to be critical in view of the axle fatigue life, because high dynamic amplification factors up to 45-50% are obtained, but on account of the localized nature and small size of this defect in this case the most severe dynamic excitation occurs at low speeds, at which the frequency of the excitation generated by the flat excites the bending resonances of the axle. For the wheel flat case, therefore, the most critical case appears to be that of freight cars, which may be often travelling at low speed.

Overall, the analyses presented in this paper show that dynamic effects are essential to correctly estimate the wheelset's fatigue life. More research and validation is needed to transfer the findings presented here into axle design practices. Hopefully however the paper has highlighted an important area for future research, in view of further improving the reliability of railway transport.

Acknowledgements

The authors gratefully acknowledge the support for this work provided by the Project TRA2010-15669 (Ministerio de Ciencia e Innovación) and TRA2007-67167 (Ministerio de Educación y Ciencia-FEDER).

References

- [1] R. A. Smith, Railway fatigue failures: an overview of a long standing problem, *Materialwissenschaft und Werkstofftechnik* 36:11 (2005) 697-705
- [2] V. Grubisic, G. Fischer, Procedure for reliable durability validation of train axles, *Materialwissenschaft und Werkstofftechnik* 37:12 (2006) 973-982
- [3] S. Beretta, M. Carboni Variable amplitude fatigue crack growth in a mild steel for railway axles: Experiments and predictive models, *Engineering Fracture Mechanics* 78 (2011) 848-862.
- [4] M. Luke, I. Varfolomeev, K. Lüthepol, A. Esderts, Fatigue crack growth in railway axles: Assessment concept and validation tests, *Engineering Fracture Mechanics* 78 (2011) 714–730.
- [5] V. Grubisic, G. Fischer, Bemessung von Radsatzwellen – Einflussgrößen und Vorgehen bei der Auslegung. Bericht FB-226, LBF, Darmstadt; 2005.
- [6] S. Alfi, F. Braghin, S. Bruni, Numerical and experimental evaluation of extreme loads for improved wheelset design, *Vehicle System Dynamics*, 46 S (2008) 431-444.
- [7] A. S. Watson, K. Timmis, A method of estimating railway axle stress spectra, *Engineering Fracture Mechanics* 78 (2011) 836–847.
- [8] S. Bruni, R. Corradi, L. Mazzola, Wheel rail contact forces as input for optimal and robust axle design, 8th International Conference on Contact Mechanics and Wear of Rail/Wheel Systems (CM2009), Firenze, Italy, September 15-18, 2009.
- [9] D.J. Thompson, C.J.C. Jones Thompson A review of the modelling of wheel/rail noise generation, *Journal of Sound and Vibration*, 231 (2000), pp. 519–536.
- [10] J.C.O. Nielsen, A. Igeland, Vertical dynamic interaction between train and track—influence of wheel and track imperfections, *Journal of Sound and Vibration* 187 (5) (1995) 825–839.
- [11] G. Diana, F. Cheli, S. Bruni, A. Collina, Experimental and numerical investigation on subway short pitch corrugation, *Vehicle System Dynamics*, 29 S, (1998) 234-245.

- 1
2
3
4
5
6
7
8
9
10
11
12
13
14
15
16
17
18
19
20
21
22
23
24
25
26
27
28
29
30
31
32
33
34
35
36
37
38
39
40
41
42
43
44
45
46
47
48
49
50
51
52
53
54
55
56
57
58
59
60
61
62
63
64
65
- [12] J.C.O. Nielsen, J. Oscarsson, Simulation of dynamic train_track interaction with state-dependent track properties, *Journal of Sound and Vibration* 275 (2004) 515–532.
- [13] J. Fayos, L. Baeza, J. E. Tarancón and F. D. Denia, An Eulerian coordinate-based method for analysing the structural vibrations of a solid of revolution rotating about its main axis, *Journal of Sound and Vibration* 306 (2007) 618–635
- [14] L. Baeza, J. Fayos, A. Roda and R. Insa, High frequency railway vehicle-track dynamics through flexible rotating wheelsets, *Vehicle System Dynamics* 46 (2008) 647 – 659
- [15] Baeza, L., Huajiang, O., A railway track dynamics model based on modal substructuring and cyclic boudary condition, *Journl of Sound and V-ibration* 330 (2011) 75-86.
- [16] L. Baeza, A. Roda, J.C.O. Nielsen, Railway vehicle/track interaction analysis using a modal substructuring approach, *Journal of Sound and Vibration* 293 (2006) 112–124
- [17] J.J. Kalker, A fast algorithm for the simplified theory of rolling contact, *Vehicle System Dynamics* 11 (1982) 1–13.
- [18] [S. L. Grassie, J. Kalousek, Rail corrugation: characteristics, causes and treatments, Proc. Instn. Mech. Engrs. Part F – Journal of Rail and Rapid Transit, 207 \(1993\), 57-68.](#)
- [19] [EN 13103 Railway applications - Wheelsets and bogies – Non-powered axles - Design method, CEN, Brussels, April 2001.](#)
- [20] [EN 13104 Railway applications - Wheelsets and bogies - Powered axles - Design method, CEN, Brussels, April 2001.](#)
- [1821] ORE B 176: Bogies with steered or steering wheelsets. Report No. 1: Specifications and preliminary studies, Vol. 2, Specification for a bogie with improved curving characteristics. ORE, Utrecht 1989.
- [2249] A. Johansson, J.C.O. Nielsen, Out-of-round railway wheels — wheel-rail contact forces and track response derived from field tests and numerical simulations, [Proc. Instn. Mech. Engrs.](#)

Part F – Journal of Rail and Rapid Transit~~Proc. IMechE Part F: J. Rail and Rapid Transit,~~
217 (2003), 135-146,~~2003~~.

1
2
3
4
5
6
7
8
9
10
11
12
13
14
15
16
17
18
19
20
21
22
23
24
25
26
27
28
29
30
31
32
33
34
35
36
37
38
39
40
41
42
43
44
45
46
47
48
49
50
51
52
53
54
55
56
57
58
59
60
61
62
63
64
65

List of figure captions

1	
2	
3	Figure 1: The train-track interaction model.
4	
5	Figure 2: The cyclic track model.
6	
7	Figure 3: Detail of the track model. Left: model of some sleeper bays. Right: sleeper and railpad
8	model.
9	
10	
11	Figure 4: Finite element model of the flexible wheelset.
12	
13	Figure 5: Studied section of wheelset and spatial point where the stresses have been calculated.
14	
15	Figure 6: Wheel-rail contact force when the vehicle circulates on a corrugated track with
16	corrugation wavelength 60 mm. Above: effect of speed and of wheelset flexibility for corrugation
17	amplitude corresponding to the ISO 3095 limit. Below: effect of corrugation amplitude for speed
18	300 km/h and flexible wheelset.
19	
20	
21	Figure 7: y-axis normal stress in the studied section of the axle (cfr. Fig. 5) when the vehicle
22	circulates on a corrugated track with corrugation wavelength 60 mm. Left: two vehicle speeds,
23	corrugation amplitude corresponding to the ISO 3095 limit. Right: two corrugation amplitudes (the
24	results are undistinguishable).
25	
26	
27	Figure 8: Wheel-rail contact force when the vehicle circulates on a corrugated track with different
28	corrugation wavelengths. Two corrugation amplitudes are considered, corresponding to the
29	ISO 3095 limit and 10 times the ISO 3095 limit. Above: the corrugation wavelength excites the
30	pinned-pinned mode of the rail. Below: the corrugation wavelength excites the first forward
31	bending mode of the wheelset.
32	
33	
34	
35	Figure 9: y-axis normal stress in the studied section of the axle (cfr. Fig. 5) when the vehicle
36	circulates on a corrugated track at 300 km/h speed. Left: the corrugation wavelength excites the
37	pinned-pinned mode of the rail. Right: the corrugation wavelength excites the first forward bending
38	mode of the wheelset.
39	
40	
41	Figure 10: Dynamic factors k_Q (vertical contact force, upper subfigure) and k_σ (y-axis stress,
42	lower subfigure) for different excitation cases and vehicle velocities. The roughness amplitude is
43	ten times higher the ISO 3095 limit.
44	
45	
46	Figure 11: Wheel-rail contact force when the vehicle circulates at 100 and 300 km/h speeds on a
47	randomly corrugated track.
48	
49	
50	Figure 12: Wheel-rail contact force when the vehicle circulates at 50 (above) and 300 km/h
51	(below) speeds on a perfectly even rail in presence of a 50 mm wheelflat.
52	
53	Figure 13: y-axis normal stress in the studied section of the axle (cfr. Fig. 5) when the vehicle
54	circulates at 300 km/h speed on a randomly corrugated track (left) and on a perfectly even rail in
55	presence of a 50 mm wheelflat at 50 km/h (centre) and 300 km/h (right).
56	
57	
58	Figure 14: Dynamic factors k_Q (vertical contact force, upper subfigure) and k_σ (y-axis stress,
59	lower subfigure) for the random corrugation and wheelflat excitation cases.
60	
61	
62	
63	
64	
65	

Table captions

Table 1: Simulation parameters.

1
2
3
4
5
6
7
8
9
10
11
12
13
14
15
16
17
18
19
20
21
22
23
24
25
26
27
28
29
30
31
32
33
34
35
36
37
38
39
40
41
42
43
44
45
46
47
48
49
50
51
52
53
54
55
56
57
58
59
60
61
62
63
64
65

Wheelset model data		Track model data	
Mass of wheelset	1375 kg	Sleeper bay	0.6 m
Axle load	120 kN	Sleeper number	70
Primary suspension longitudinal stiffness	7.5 MN/m	Sleeper mass	324 kg
Primary suspension lateral stiffness	7.1 MN/m	Track bed stiffness	200 MN/m
Primary suspension vertical stiffness	0.81 MN/m	Track bed damping	150 kNs/m
Primary suspension vertical damping	30 kNs/m	Rail pad stiffness	1 GN/m
Primary suspension longitudinal damping	100 kNs/m	Rail pad damping	50 kNs/m
Primary suspension lateral damping	100 kNs/m	Rail section	UIC60

Table 1: Simulation parameters.

Figure 1

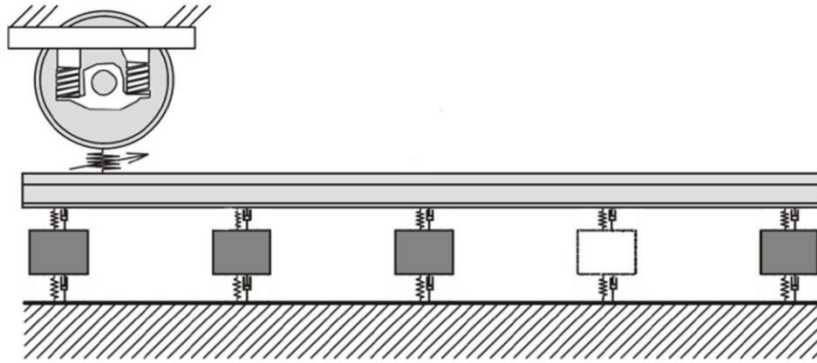


Figure 1: The train-track interaction model.

Figure 2

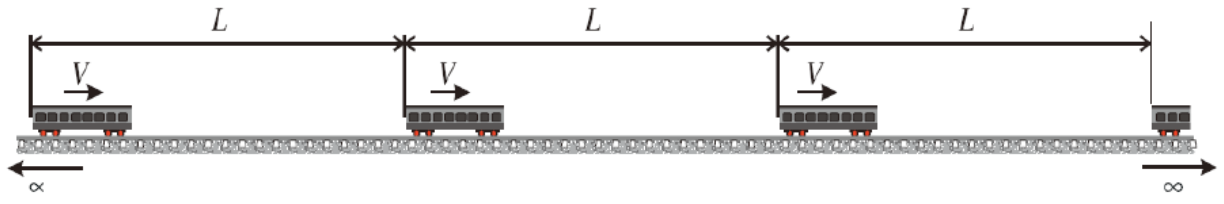


Figure 2: The cyclic track model.

Figure 3

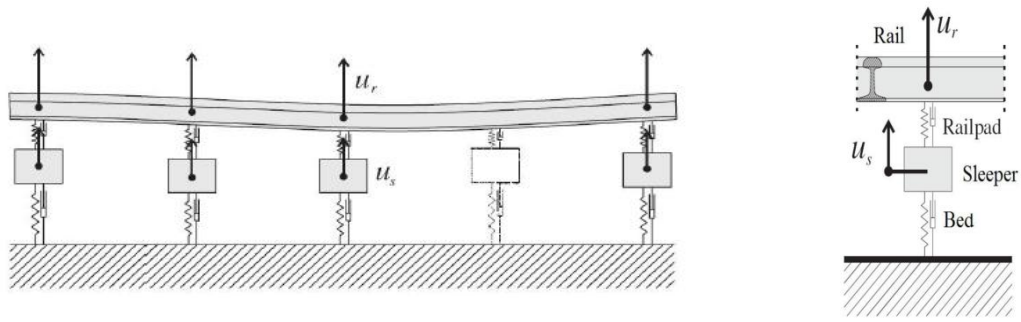


Figure 3: Detail of the track model. Left: model of some sleeper bays. Right: sleeper and railpad model.

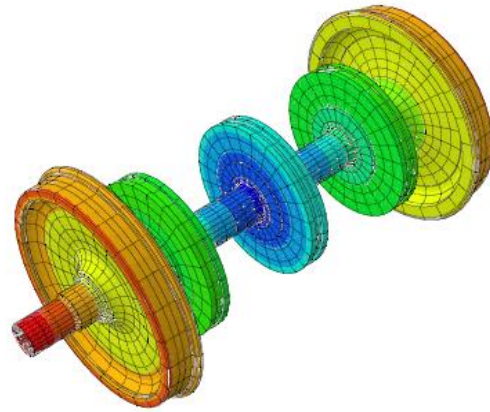


Figure 4: Finite element model of the flexible wheelset.

Figure 5

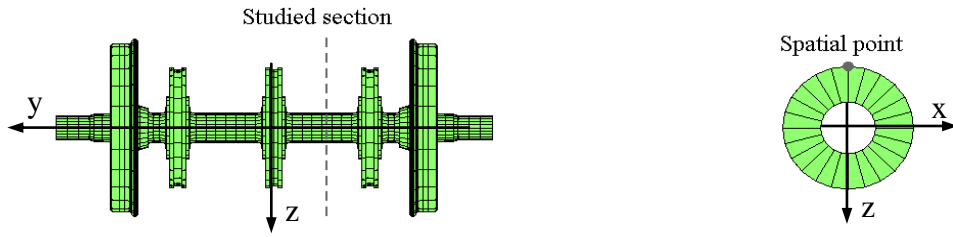


Figure 5: Studied section of wheelset and spatial point where the stresses have been calculated.

Figure 6

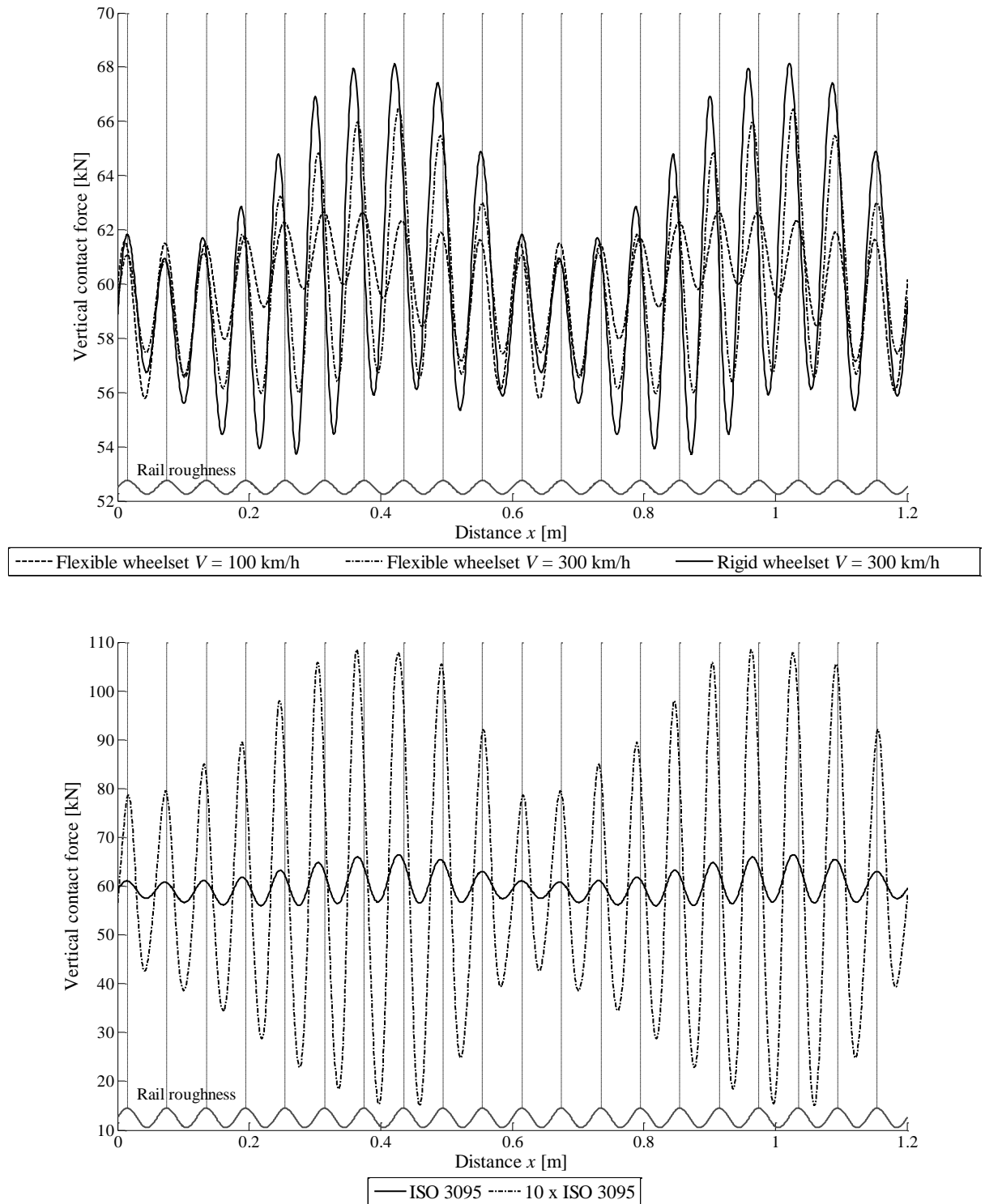


Figure 6: Wheel-rail contact force when the vehicle circulates on a corrugated track with corrugation wavelength 60 mm. Above: effect of speed and of wheelset flexibility for corrugation amplitude corresponding to the ISO 3095 limit. Below: effect of corrugation amplitude for speed 300 km/h and flexible wheelset.

Figure 7

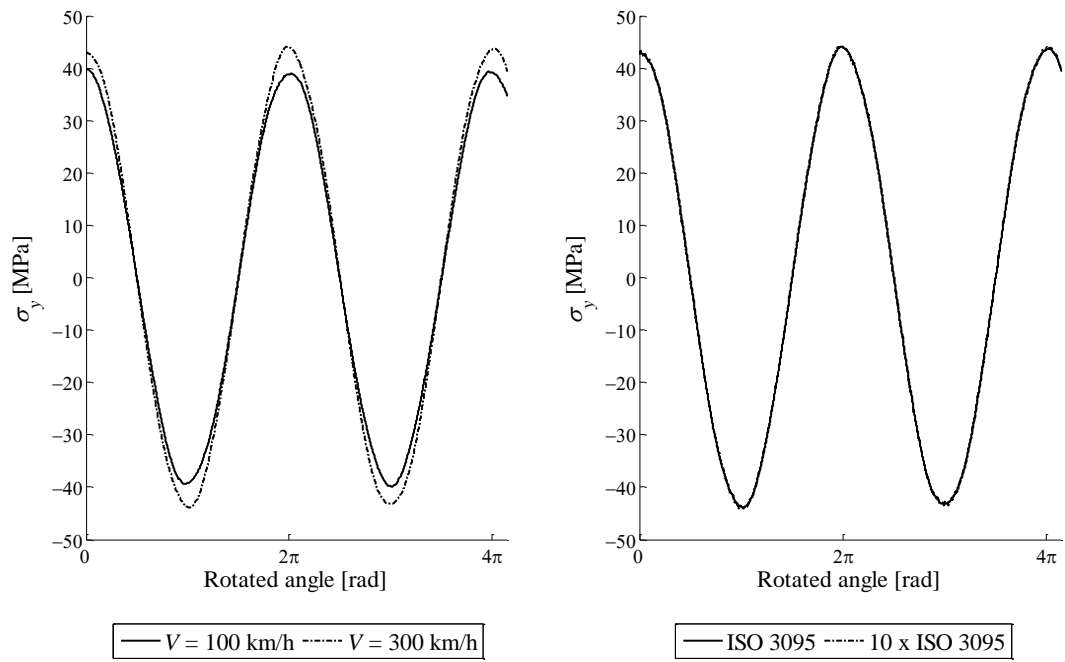


Figure 7: y-axis normal stress in the studied section of the axle (cfr. Fig. 5) when the vehicle circulates on a corrugated track with corrugation wavelength 60 mm. Left: two vehicle speeds, corrugation amplitude corresponding to the ISO 3095 limit. Right: two corrugation amplitudes (the results are undistinguishable).

Figure 8

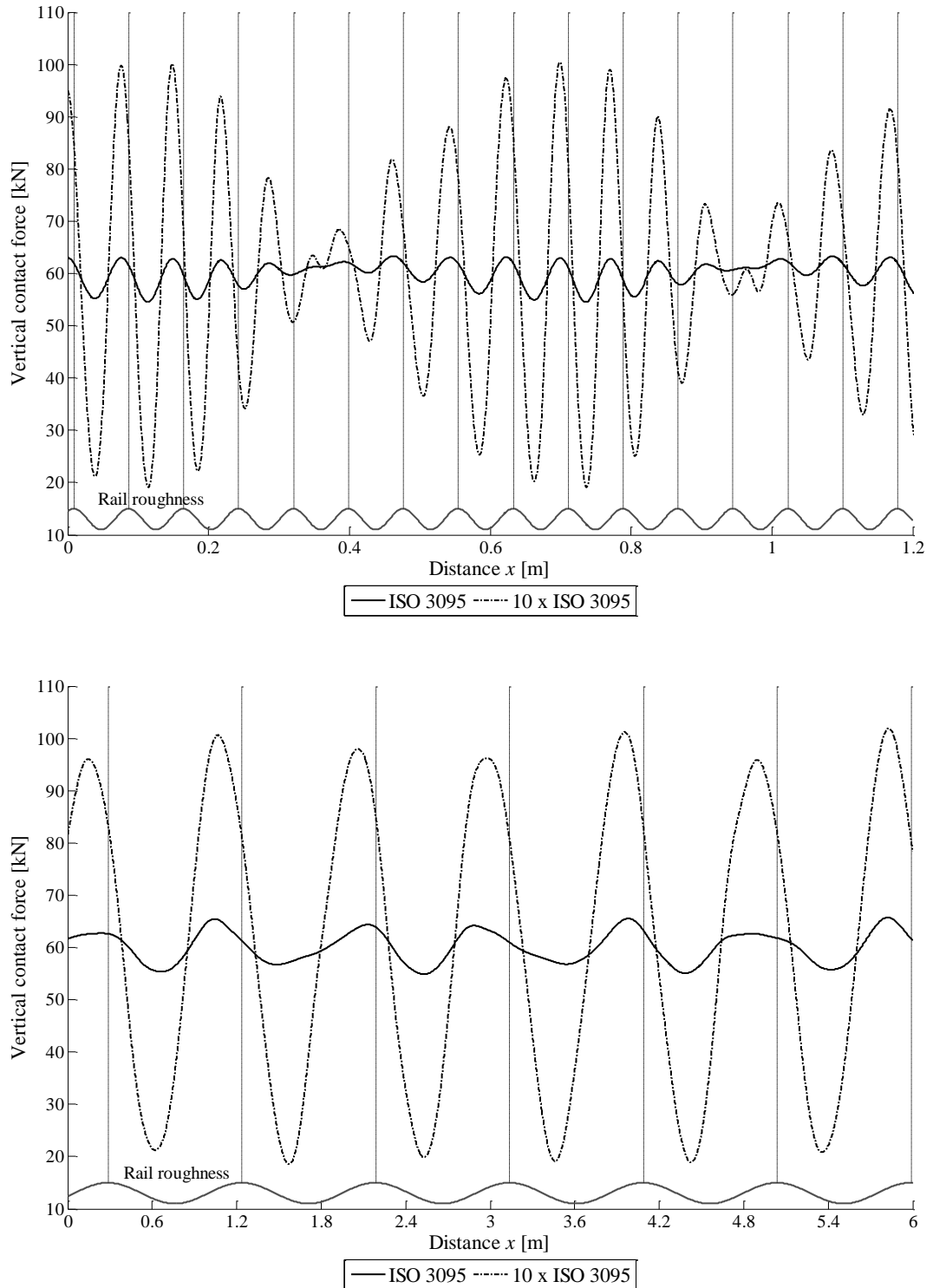


Figure 8: Wheel-rail contact force when the vehicle circulates on a corrugated track with different corrugation wavelengths. Two corrugation amplitudes are considered, corresponding to the ISO 3095 limit and 10 times the ISO 3095 limit. Above: the corrugation wavelength excites the pinned-pinned mode of the rail. Below: the corrugation wavelength excites the first forward bending mode of the wheelset.

Figure 9

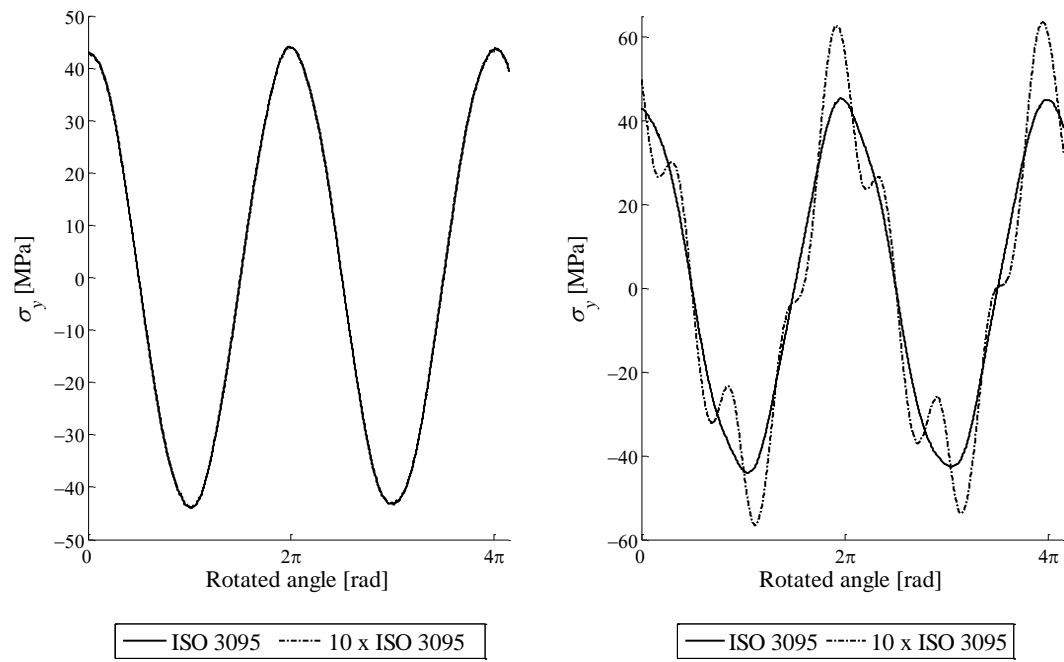


Figure 9: y-axis normal stress in the studied section of the axle (cfr. Fig. 5) when the vehicle circulates on a corrugated track at 300 km/h speed. Left: the corrugation wavelength excites the pinned-pinned mode of the rail. Right: the corrugation wavelength excites the first forward bending mode of the wheelset.

Figure 10

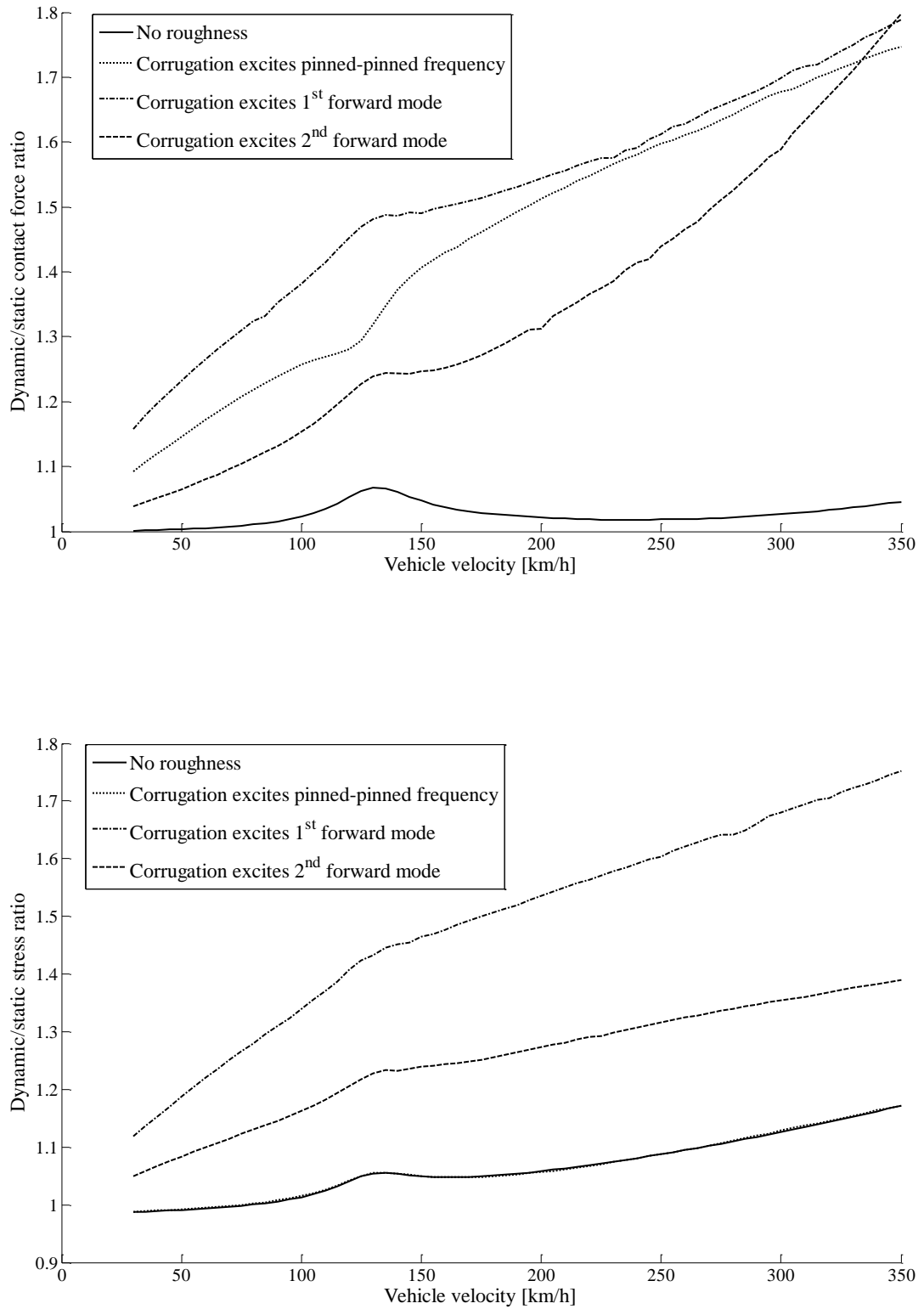


Figure 10: Dynamic factors k_Q (vertical contact force, upper subfigure) and k_σ (y-axis stress, lower subfigure) for different excitation cases and vehicle velocities. The roughness amplitude is ten times higher the ISO 3095 limit.

Figure 11

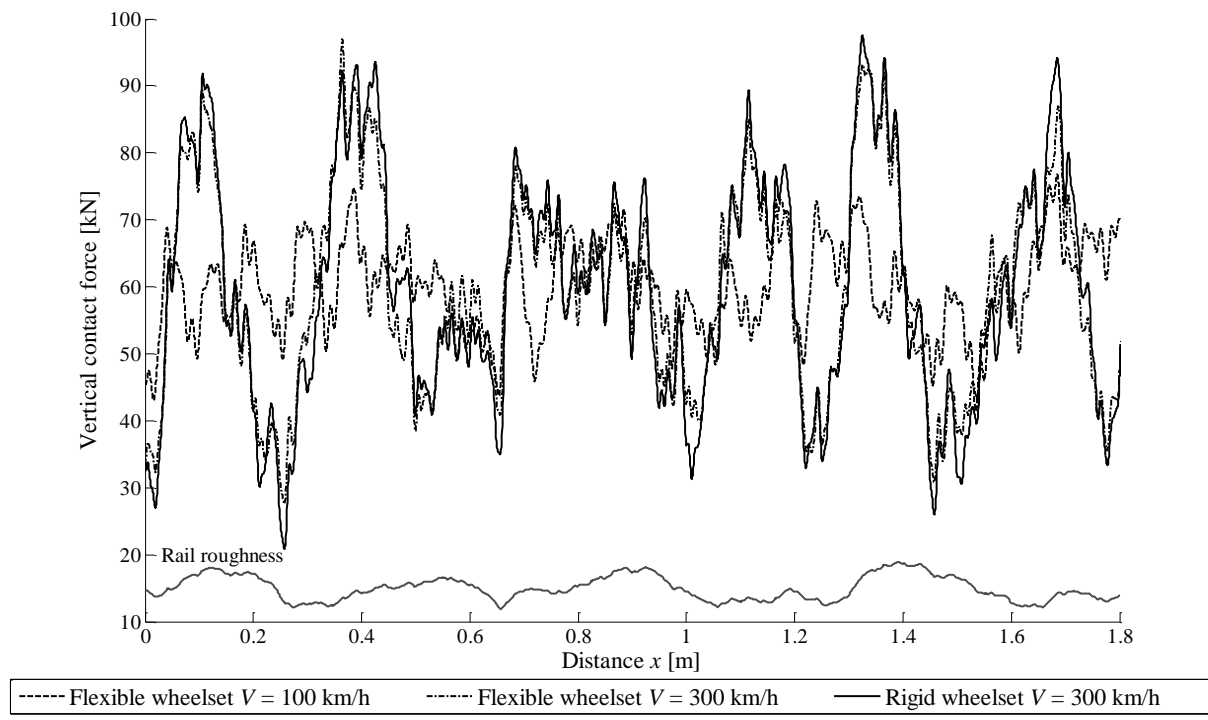


Figure 11: Wheel-rail contact force when the vehicle circulates at 100 and 300 km/h speeds on a randomly corrugated track.

Figure 12

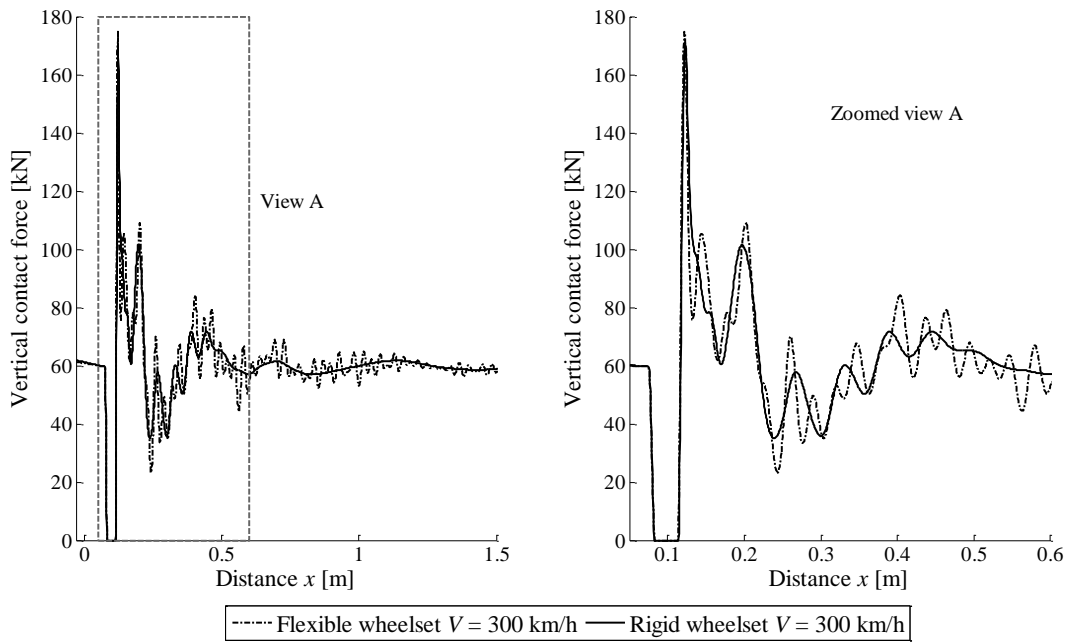
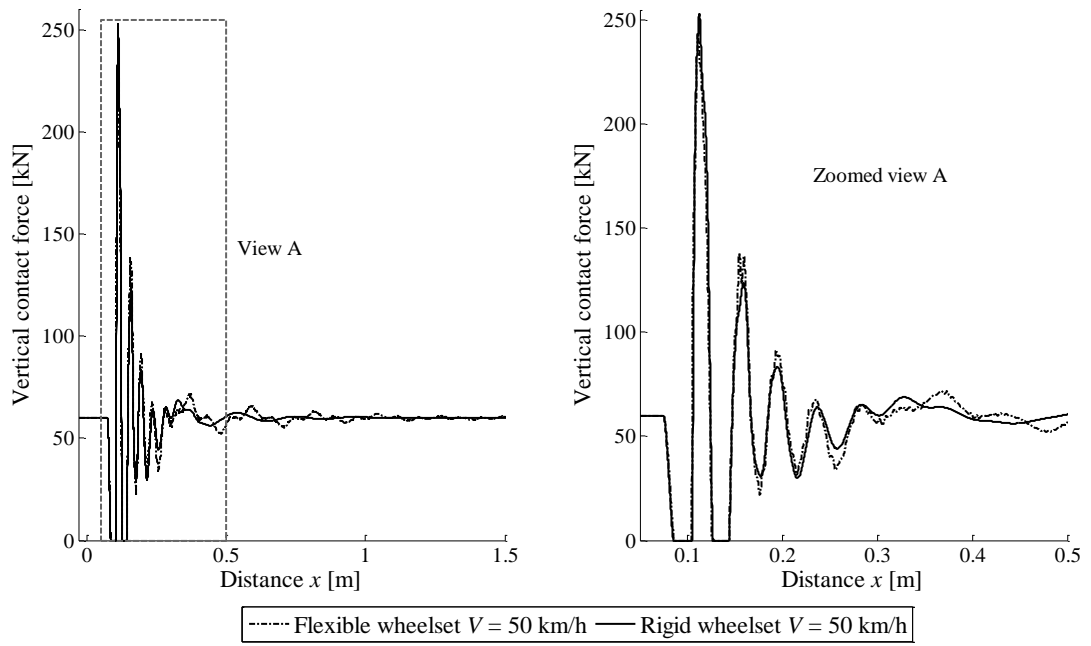


Figure 12: Wheel-rail contact force when the vehicle circulates at 50 (above) and 300 km/h (below) speeds on a perfectly even rail in presence of a 50 mm wheelflat.

Figure 13

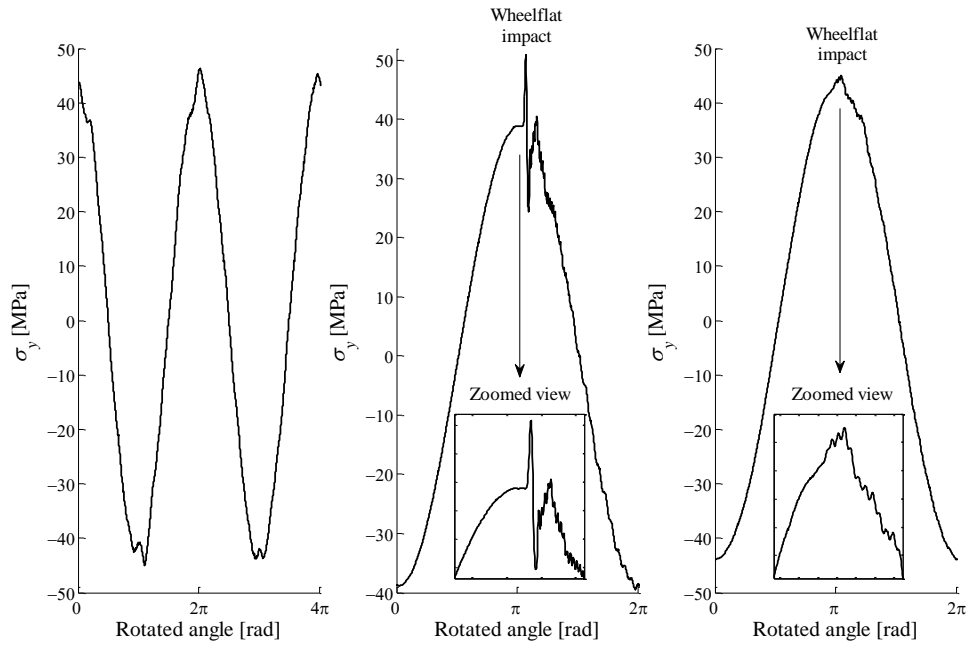


Figure 13: y-axis normal stress in the studied section of the axle (cfr. Fig. 5) when the vehicle circulates at 300 km/h speed on a randomly corrugated track (left) and on a perfectly even rail in presence of a 50 mm wheelflat at 50 km/h (centre) and 300 km/h (right).

Figure 14

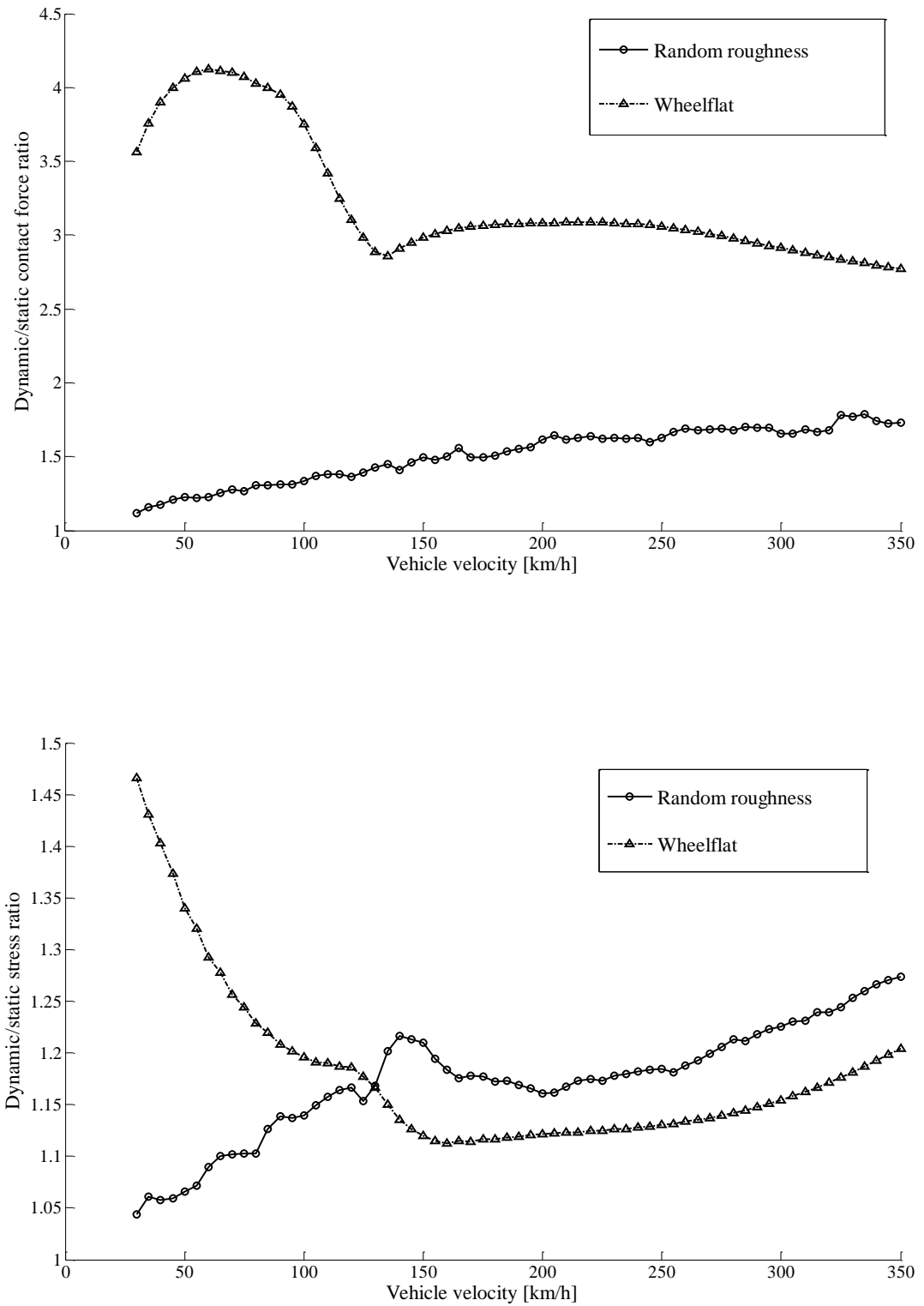


Figure 14: Dynamic factors k_Q (vertical contact force, upper subfigure) and k_σ (y-axis stress, lower subfigure) for the random corrugation and wheelflat excitation cases.